High performance room temperature p-type injection in few-layered tungsten diselenide films from cobalt and palladium contacts

Jacko Rastikian, Stéphan Suffit, Pascal Martin, Philippe Lafarge, Odile Bezencenet, Maria Luisa Della Rocca, Clement Barraud

Materials Research
Express

PAPER • **OPEN ACCESS**

High performance room temperature p-type injection in few-layered tungsten diselenide films from cobalt and palladium contacts

To cite this article: Jacko Rastikian *et al* 2019 *Mater. Res. Express* **6** 126307

Materials Research Express

PAPER

High performance room temperature p-type injection in few-layered tungsten diselenide films from cobalt and palladium contacts

Jacko Rastikian[1,4], **Stéphan Suffit**[1], **Salvatore Timpa**[1], **Pascal Martin**[2], **Philippe Lafarge**[1], **Odile Bezencenet**[3], **Maria Luisa Della Rocca**[1] and **Clément Barraud**[1,4]

[1] Université de Paris, Laboratoire Matériaux et Phénomènes Quantiques, CNRS, F-75013 Paris, France
[2] Université de Paris, Laboratoire ITODYS, CNRS, F-75013 Paris, France
[3] Thales Research and Technology, F-91767 Palaiseau, France
[4] Authors to whom any correspondence should be addressed.

E-mail: clement.barraud@univ-paris-diderot.fr **and** jacko.rastikian@univ-paris-diderot.fr

Keywords: WSe_2, palladium, cobalt, charge injection, holes transport

Supplementary material for this article is available online

OPEN ACCESS

RECEIVED
23 September 2019

REVISED
17 October 2019

ACCEPTED FOR PUBLICATION
12 November 2019

PUBLISHED
27 November 2019

Abstract

Field-effect electronic devices based on transition metals dichalcogenides (TMDs) have recently received a tremendous interest. Although widely studied, efficient charge injection in those materials is often impeded by the large injection barrier present at the interface between the electrode and the TMD, in particular when holes transport is needed. In this paper, e-beam lithography and e-beam evaporation techniques are used to contact few-layered WSe_2 films with patterned metallic electrodes (Co and Pd).. We measured the transport and the injection properties at various gate voltages, source-drain voltages and different temperatures. A quantitative analysis is performed using a two-dimensional version of a thermionic emission model to extract the evolution of the injection barrier height as a function of the gate voltage. Palladium contacts are found to be very transparent in the hole injection regime but weakly tunable under the application of a gate voltage. Cobalt contacts present a low injection barrier which, unlike Pd contacts, can be extremely reduced by electrostatic gating. In both cases low injection barriers with respect to the literature are extracted. These results demonstrate a solid potential for applications implying WSe_2 in the hole transport regime. The results reveal also an excellent agreement when compared to previous theoretical studies by taking into account the role of hybridized interfacial states and of the spin–orbit coupling of the contacting material on the injection barrier.

Introduction

Two-dimensional (2D) materials are fascinating for the novel physics they offer [1, 2]. Their unique electrical, optical and mechanical properties continuously open a promising panel of new applications such as vertically architectured transistors [3] or highly-tunable opto-electronics devices [4]. In the wide family of existing 2D materials, recently discovered transition metal dichalcogenides (TMDs) [5] exhibit a notable variety of interesting properties for combining opto-electronics [6, 7], spintronics [8, 9] and electronics applications [10–13]. The main reason is that unlike classical materials in thin films such as metals, oxides and semiconductors based on Si, GaAs, and others, TMDs are characterized by a fully controllable electronic structure [14, 15] down to an atomically thin thickness. Tungsten diselenide (WSe_2), a representative TMD, is a semiconductor with a direct band gap of 1.6 eV for one monolayer (ML) and an indirect gap of 1.2 eV in its bulk form [16]. It is also characterized by a large spin–orbit coupling (SOC) making it an interesting material for spin and valley physics [17–19]. Thanks to its large band gap and relatively high carrier's mobility, WSe_2 is also a promising material for field effect transistors (FET) with high On/Off ratio [20, 21].

2D-based FETs properties are known to be very dependent on the electronic properties of the microscopic metal/semiconductor interface. The presence of a metal in contact with WSe_2 is known to impact the electronic

properties of both materials [14, 22]. This is due to the formation of chemical bonds and defects that could lead to gap states and thus to Fermi level pinning [23, 24], and to charge transfer and screening [25]. The presence of those effects and their respective amplitude can depend not only on the deposited metals, but also on the deposition techniques and parameters [26]. As a general consequence, an injection barrier such as a Schottky barrier is induced on the TMD's side [27, 28] and is known to also vary with the number of layers composing the connected TMD [29]. Those effects can be probed and quantified thanks to electronic transport measurements. A large contact resistance (i.e. a large injection barrier), for instance, prevents FET's good performance in the high-frequency regime [22, 30]. This contact resistance is related to the density of states and to the work function (WF)

of the metal. More specifically, it is influenced by the relative position between the contact's Fermi level and the energy bands of the semiconductor. In this sense, a precise alignment of the metal's Fermi energy within one of the bands of the semiconductor is generally preferred to promote transparent contacts. Achieving efficient holes carriers' injection through p-type metallic contacts in WSe_2 concentrates a considerable effort for two main reasons [31]. First, WSe_2 prefers p-type doping unlike other TMDs like MoS_2 [21, 32–34] and holes shows high mobilities up to 4 000 $cm^2/V.s$ [35]. Second, due to its strong SOC, WSe_2 is characterized by a large spin-splitting of the valence band maximum of the order of 460 meV in a monolayer (ML) WSe_2. This makes such a material highly sought-after for opto-spintronics applications [9, 36].

In this work, we study metal-WSe_2 contact properties for metallic electrodes with high work functions (Co, Pd) within the hole transport regime. We also compare their efficiency at room temperature with an intermediate work-function metal (Ti) showing poor injection properties. We demonstrate a direct correlation between the chosen metal and the injection barrier. To clarify this link, we study both the gate voltage and the temperature dependence of the device resistance including the different contact resistance, showing that devices with Co- and Pd-based contacts are the best candidates to implement holes transport in WSe_2.

Results and discussions

WSe_2- based device's micro-fabrication

Figure 1 highlights different characterizations performed on WSe_2 deposited on a Si/SiO_2 commercial wafer demonstrating its excellent physical properties. Figure 1(a) shows an optical image of mechanically exfoliated WSe_2 flakes from a bulk p-doped crystal over a SiO_2 (280 nm)/Si wafer. The thickness of the SiO_2 is chosen to maximize the contrast between WSe_2 sheets of different thicknesses down to a monolayer [37, 38]. Then we performed atomic force microscopy (AFM) in the tapping mode to determine their thickness and their surface topography, as shown in figure 1(b). The lateral profile plotted in figure 1(c) is obtained along a single line cut shown on the AFM image. The thickness of the WSe_2 is identified in this particular case to be 3.5 nm, which corresponds to a 5-layers film. The surface roughness of WSe_2 is of the same order of magnitude of that of SiO_2 (i.e. <1 nm) emphasizing the excellent surface quality. Some recent methods of fabrication, for instance by encapsulating WSe_2 between relatively thick BN sheets, could help reducing this surface roughness down to the angstrom level [39–41]. We also performed Raman spectroscopy measurements to get a better insight in the electronic properties [42, 43]. On the Raman spectra shown in figure 1(d), a large resonance can be seen around 255 cm^{-1}. This peak corresponds to the labelled LA(M) peak containing both the A_{1g} and the E_{2g} transitions [44]. The A_{1g} peak is very sharp (<5 cm^{-1}) and is located around 251 cm^{-1} and the E^1_{2g} peak is centered on 248 cm^{-1}, the resolution of our measurements does not allow to fully split them. The position of the different Raman transition's peaks confirm the material's high quality and its few-layered character [45]. A photoluminescence spectra of a multilayer WSe_2 flake is also shown in figure 1(e). It provides the energy of the direct band gap (1.6 eV) and the energy of the indirect band gap (1.4 eV) which are in perfect agreement with previous measurements [46, 47]. The field-effect device is finally fabricated by defining electrical contacts by e-beam lithography as described in the methods section. Figure 2 shows an AFM image of a final device made of few layered WSe_2 of typical lateral sizes of 10 μm. The metallic contacts serve as source and drain, while the gate voltage is applied to the Si back-gate. Both Ti and Pd based devices were fabricated over a 280 nm thick SiO_2 and the Co based device was fabricated over a 100 nm thick SiO_2 in order to get a larger electrostatic coupling. In all the studied devices, the WSe_2 flakes are composed of few layers with thicknesses around 3.5–4 nm.

Influence of the contacts on charge injection in WSe_2

Figure 3(a) shows the WSe_2 band gap indicating the positions of the top of the valence band (E_V) and of the bottom of the conduction band (E_C) [48] and the work functions of the metals used as electrical contacts in this study [49]. By comparing the relative positions of the different work functions to the position of the valence band maximum, it is expected that Co and Pd greatly favor holes injection and transport. We now focus on the two-terminal I_{SD}–V_{SD} characteristics measured at $V_G = 0$ V and at room temperature for Ti (black dots), Co (red

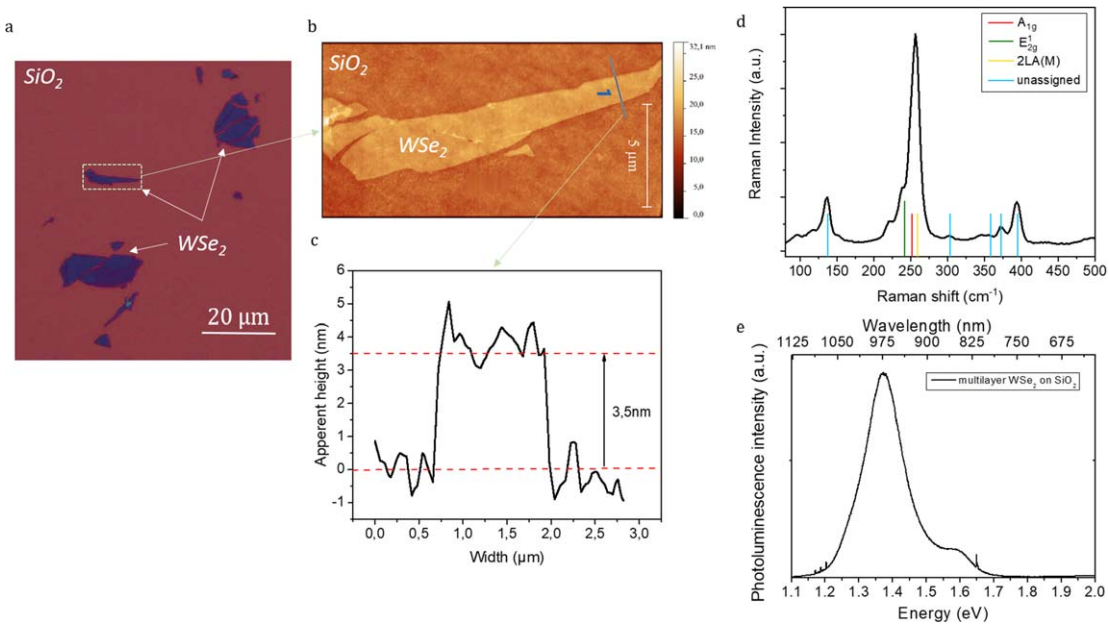

Figure 1. (a) Optical microscope image of multiple WSe_2 flakes exfoliated over a Si/SiO_2 (280 nm) substrate. (b) Atomic force microscope image obtained in the tapping mode of an individual WSe_2 flake. (c) Profile obtained along the line cut indicated in blue over the WSe_2 flake. The thickness of the flake is measured to be 3.5 nm. (d) Raman spectra obtained on the WSe_2 flake ($\lambda = 633$ nm, $P = 2$ mW). Resonances attributed to A_{1g}, E_{2g} and 2LA are identified by red, green and yellow lines respectively. Unassigned resonances are also marked (they are also reported in [44]). (e) Photoluminescence spectra ($P = 0.1$ mW and $\lambda_{exc} = 514$ nm) of a multilayer WSe_2 flake deposited on a SiO_2 substrate. The indirect band gap peak is centered on 1.4 eV and the direct band gap peak is centered on 1.6 eV.

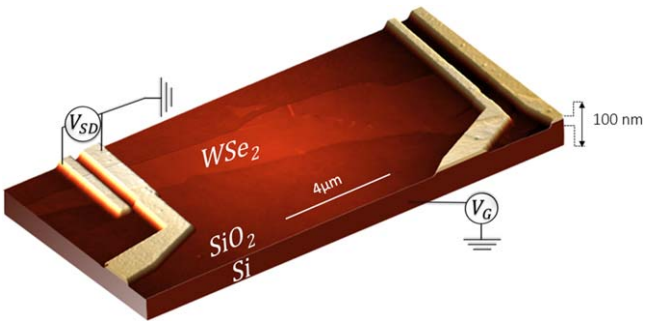

Figure 2. Three-dimensional atomic force image of a final device with four Ti (5 nm)/Au (95) electrodes. The wiring of the device is also schematized with the two different voltage sources (source-drain voltage V_{SD} and gate voltage V_G).

dots) and Pd (blue dots) contacts plotted in figure 3(b). Because of this specific configuration, the measured signal can include contributions of the contact resistances and the channel resistance. As reported, for Ti contacts, the current level is very weak reaching a few hundreds of pA, while a current up to 20 nA is observed for the device with Co contacts at $V_{SD} > 2$ V. On the other hand, the blue curve on figure 3(b) shows for the Pd contacts a current two orders of magnitude higher than that for the devices with Co contacts. These measurements illustrate also asymmetric and non-linear characteristics at high bias voltages (>0.2 V). As illustrated in figures 4(a)–(f), we also observe that the current remains rather weak around $V_{SD} = 0$ V for Co contacts in contrast to Pd contacts at any explored temperature. As an example, at 300 K and for $V_{SD} = 0.2$ V, I_{SD} is ~0.5 nA for Co contacts and ~31 nA for Pd contacts as extracted from figure 3(b). Zooms at low bias voltages (<0.2 V) are also plotted for Pd contacts in figure S1 is available online at stacks.iop.org/MRX/6/126307/mmedia highlighting the linear variation of I_{SD} with respect to V_{SD}. For both devices based on Pd and Co contacts, I_{SD} increases drastically for $|V_{SD}| > 2$ V when applying negative gate voltages. The behavior of devices based on Pd and Co contacts are in agreement with expectations in the case of holes injection [32]. This is also confirmed by the two I_{SD}-V_G characteristics (in figure 3(c)) obtained at 3 K shown for Co contacts (in red) and Pd contacts (in blue) based devices. Interestingly, we clearly notice the valence band edge for Co contacts at $V_G = -8$ V whereas it is very diffuse for the Pd contacts.

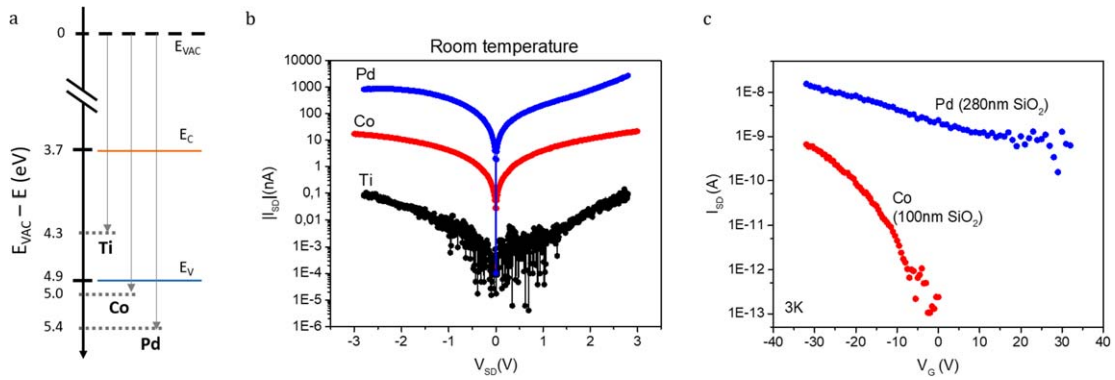

Figure 3. (a) Band alignment with respect to the vacuum level of the bottom of the conduction band (orange line at 3.5 eV) and top of the valence band (blue line at 4.9 eV) for WSe_2 and the Fermi energy positions for Ti (4.3 eV), Co (5 eV) and Pd (5.4 eV) [48, 49]. (b) Room temperature I_{SD}–V_{SD} characteristics obtained at zero gate voltage on devices with Ti (black), Co (red) and Pd (blue) contacts over a 280 nm SiO_2 substrate. (c) I_{SD}-V_G characteristics measured for $V_{SD} = -2$ V at 3 K for Co contacts (red) and Pd contacts (blue).

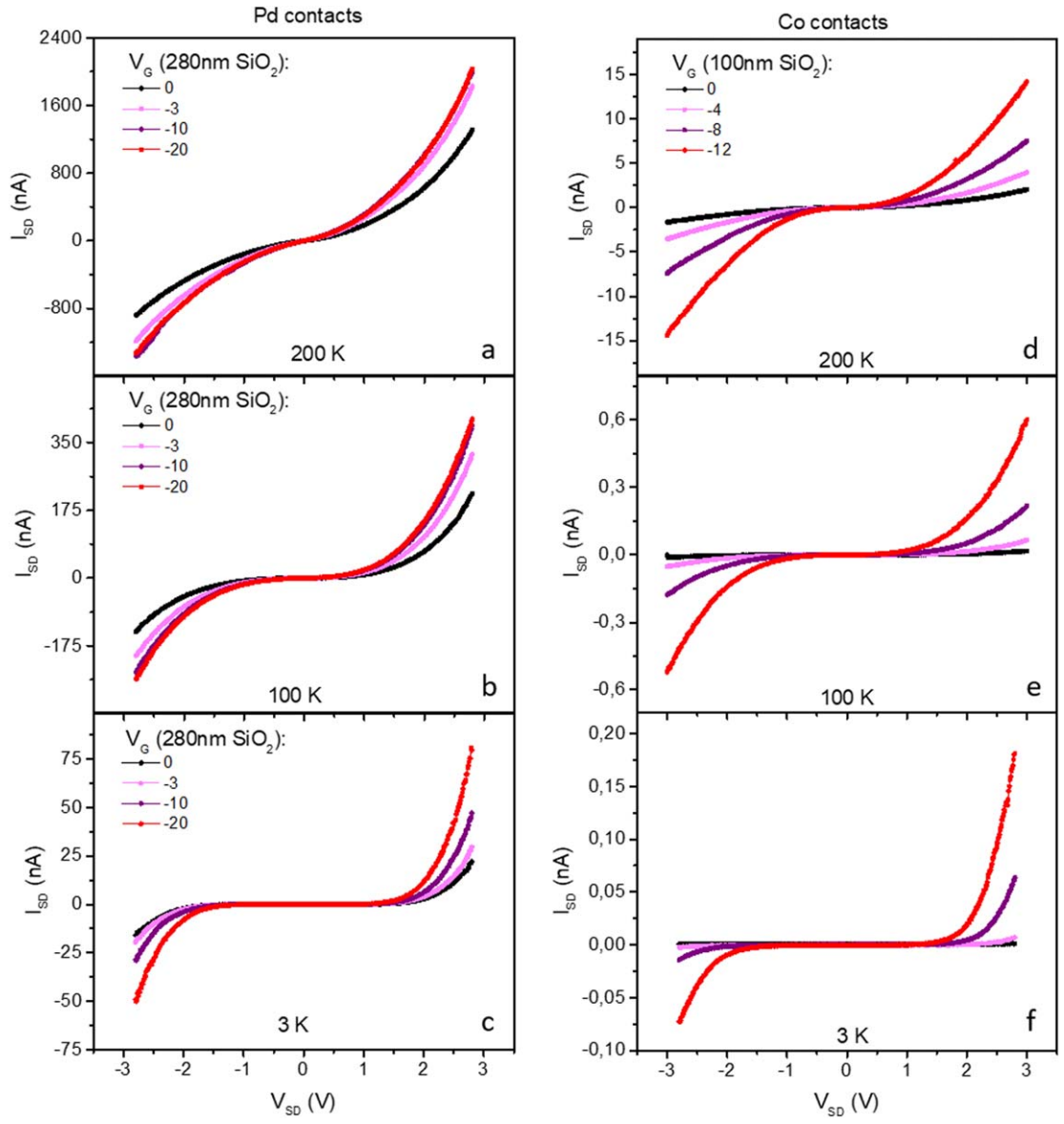

Figure 4. I_{SD}–V_{SD} characteristics obtained at different gate voltages on a device with Pd (and Co) contacts over a 280 nm (100 nm) SiO_2 substrate for temperatures of a, (d) 200 K (up), b, (e) 100 K (middle) and c, (f) 3 K (down).

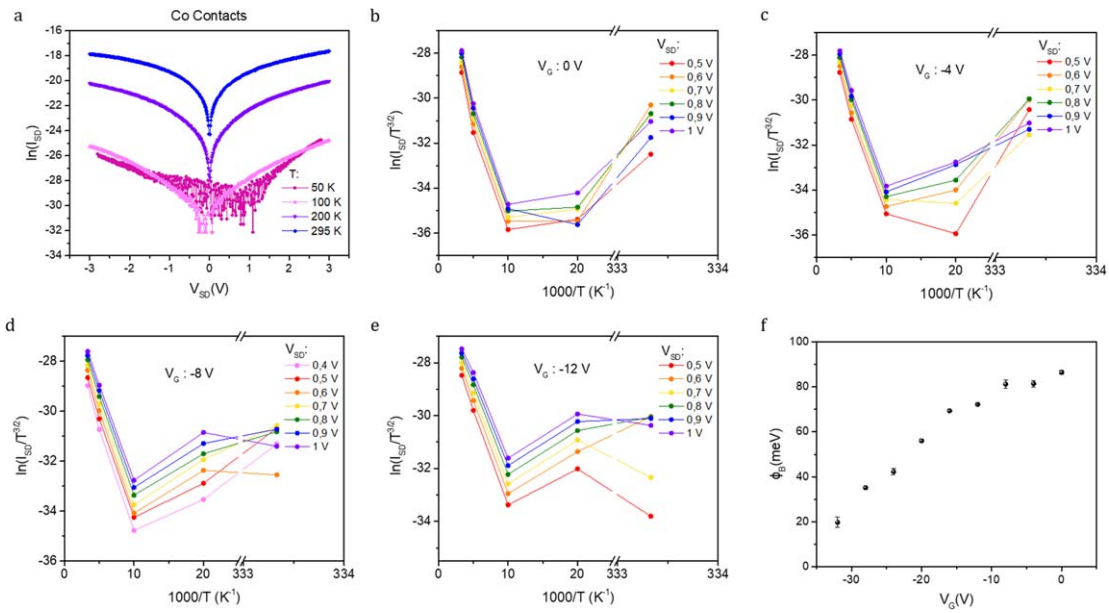

Figure 5. (a) I_{SD}–V_{SD} characteristics in semi-log scale measured at zero gate voltage at four different temperatures ranging from 3 K to 295 K for the Co-based device. (b)–(e) $\ln(I_{SD}/T^{3/2}) = f(1000/T)$ plots performed at $V_G = 0$ V, −4 V, −8 V and −12 V respectively. (f) Evolution of the injection barrier height for holes (ϕ_B) as a function of the gate voltage (V_G).

To summarize this part, in devices with Pd contacts a stronger current (i.e. more transparent contacts) is observed with respect to devices with Co or Ti contacts. This can be understood by looking at the band diagram presented in figure 3(a). The Ti Fermi level falls deep in the band gap of WSe_2, which indeed creates a large injection barrier, while the Co and Pd Fermi levels fall deep inside the valence band of the WSe_2, strongly promoting hole injection.

Electrostatic gating effect on the injection barrier height

To investigate in more details the charge injection properties, we present in figures 5(a) and 6(a) the I_{SD}–V_{SD} characteristics measured at different temperatures ranging from room temperature to 50 K at $V_G = 0$ V for the Co-based device and the Pd-based device respectively in a two-terminal configuration. Given the poor transparency of the Ti contacts, we discharge these devices from the following analysis. The plots reveal a general decrease of the current when decreasing the temperature, meaning that the charge transport process is thermally activated. From figure 5(a) we remark that the symmetry of the Co two-terminal I_{SD}–V_{SD} characteristics plot is preserved at all temperatures. For the Pd contacts, the symmetry is broken at room temperature as shown in figure 6(a), due to the presence of a negative differential resistance (NDR) signature at negative polarization. NDR has already been reported in WSe_2-based FET with Pt contacts [35], even if not systematically. It has been shown to be strongly gate voltage dependent and it has been interpreted as the effect on charge transport of the V_G-induced change of the vertical carrier distribution across the different layers composing the connected WSe_2 flake.

In order to get a deeper understanding of the charge injection process with Co and Pd contacts, we perform a full temperature study. Figures 5(b) to (e) and 6(b) to (e) present the temperature and the gate dependence of the current (I_{sd}) applied to the device through Co and Pd contacts respectively for different applied voltage bias ($V_{sd} > 0.5$ V).

A quantitative description of the injection properties in ultrathin 2D materials is given by a 2D thermionic emission equation [50], where the expression of I_{SD} employs a reduced power-law $T^{3/2}$:

$$I_{SD} = A^*_{SD} S T^{3/2} \exp\left[-\frac{1}{k_B T}\left(\varphi_B - q\frac{V_{SD}}{n}\right)\right],$$

where A^*_{SD} is the 2D equivalent Richardson constant, q the elementary charge, S the contact area, T the temperature, k_B the Boltzmann constant and n is the ideality factor. This model has been developed for symmetric metal/2D semiconductor/metal devices and is commonly employed, when the device is sufficiently polarized, for characterizing only one over two injection barriers in FET devices [30] based on a TMD [51–53] channel. The model is also used even in the limit of very transparent metal/TMD or metal/h-BN/graphene contacts [54, 55], where a substantial part of the potential drop could occur within the semiconducting channel itself. Reference [30] fully details the validity of this method. In accordance with this method, we restrain this

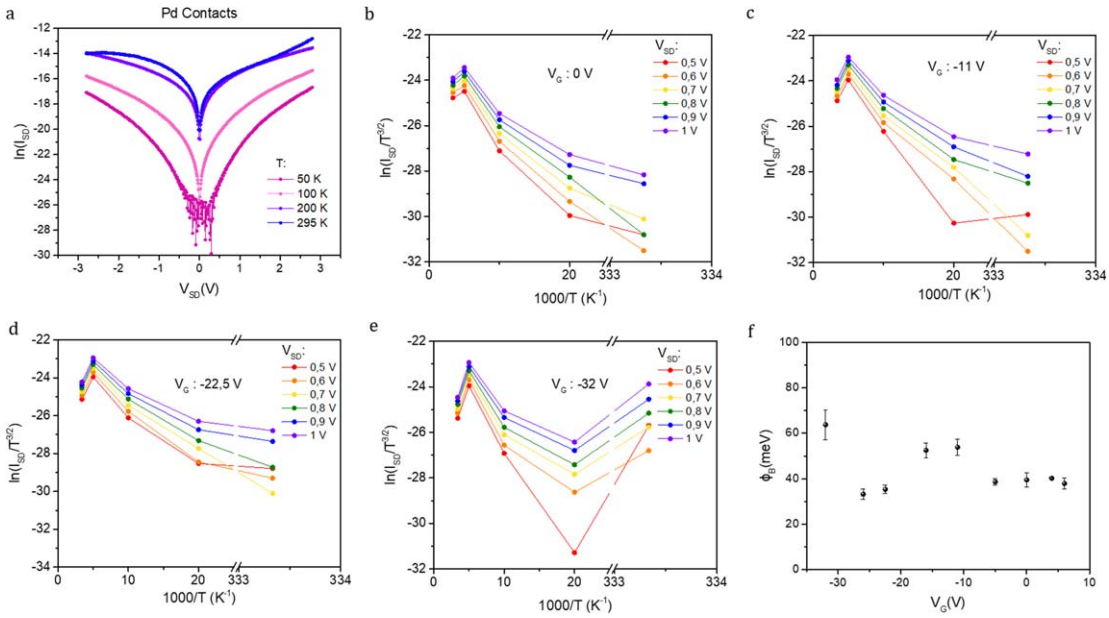

Figure 6. (a) I_{SD}–V_{SD} characteristics in ln scale measured at zero gate voltage at four different temperatures ranging from 50 K to 295 K for the Pd-based device. (b), (c), (d) and (e) $\ln(I_{SD}/T^{3/2}) = f(1000/T)$ plots performed at $V_G = 0$ V, −11 V, −22.5 V and −32 V respectively. (f) Evolution of the injection barrier height for holes (ϕ_B) as a function of the gate voltage (V_G).

study to $V_{SD} > 0.5$ V in order to ensure that only one barrier mainly contribute to the measured signal as it is discussed in [30]. To determine the height of the injection barrier (φ_B) as a function of V_G, Richardson plots of $\ln(I_{SD}/T^{3/2})$ against $1000/T$ at different applied V_G for both Co and Pd based devices are shown in figures 5 and 6, from b to e, respectively. For each value of V_{SD} we realize a linear fit in the high temperature regime (between 300 K and 100 K for the Co based devices and between 200 K and 50 K for the Pd based devices). We exclude the room temperature measurement for the Pd-based device where the NDR effect dominates. The slope extracted from the linear fit is given by:

$$a = -\frac{1}{1000k_B}\left(\varphi_B - q\frac{V_{SD}}{n}\right).$$

By plotting the slopes as a function of V_{SD}, we can extract the injection barrier height from the y-intercept as [56]:

$$a_0 = -\frac{1}{1000k_B}(\varphi_B).$$

The extracted injection barrier heights with their standard deviations are plotted as a function of the applied gate voltage V_G and on figures 5(f) and 6(f) for the Co and Pd based devices respectively. The barrier height decreases from 90 meV down to 20 meV in the Co-based device when the gate voltage is lowered from 0 V to −32 V. In the Pd-based device, the barrier height is already lower at low gate voltages and remains stable around 40 meV at negative gate voltages. The extracted values of the injection barrier at zero gate voltage are plotted and compared to the literature for different contact materials in figure 7. The comparison with experimental data reported at zero gate voltage by Kim *et al* [57] reveals a large discrepancy but those data have been measured with chemical vapor deposited WSe_2 for which the intrinsic doping might be very different than after exfoliation from a bulk crystal. Note that a perfect agreement exists between our observations and the theoretical predictions made by Wang *et al* [31] for the Pd contacts based devices, including the influence of spin–orbit coupling which tends to shift the valence band closer to the metal's Fermi energy. The Schottky-Mott rule ($\varphi_B = |WF - 4.9|$) is also plotted as a reference.

Discussion

The method we employed to extract the injection barrier in two-terminal 2D material based devices is standardly used in the literature [58]. Three distinct injection regimes can usually be identified depending on the gate voltage V_G. A thermionic emission regime is associated to a linear decrease of φ_B as a function of V_G, a tunneling regime is associated to an almost stable φ_B as a function of V_G and, in between, a crossover regime is ascribed as

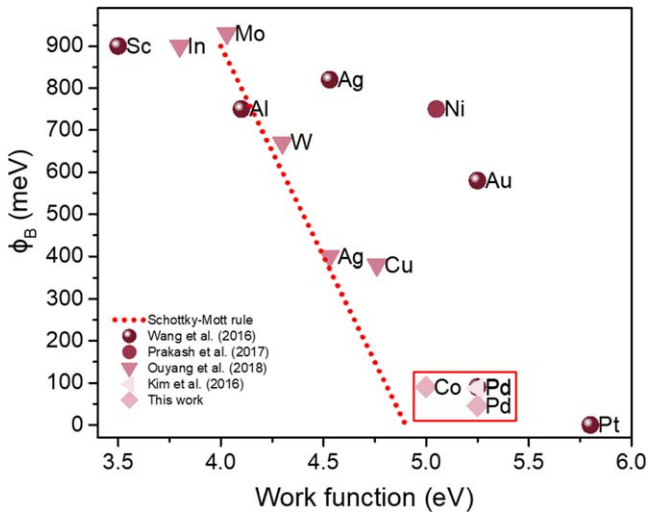

Figure 7. Holes injection barrier ϕ_B (in meV) as a function of work function (in eV) for different materials. Calculated hole injection barriers (purple dots from Wang *et al* [31] and pink triangles from Ouyang *et al* [25]) and measured hole injection barriers (red dots from Prakash *et al* [28], light pink triangles from Kim *et al* [57] and the pink diamonds from this work) are represented. The standard Schottky-Mott rule is plotted (red dotted line) for reference.

the flat band limit for which both thermionic and tunneling injection can occur simultaneously [32, 59]. The intrinsic Schottky barrier height can only be determined at the flat band limit [30]. For the case of the Co contacts based device, we observe a decreasing behavior of the injection barrier while increasing the gate voltages towards negative values, as shown in figure 5(f). This is expected since, based on the energy level alignments, Co contacts are supposed to promote holes injection in WSe_2. In the studied experimental conditions, this injection barrier decreases down to 20 meV at $V_G = -30$ V. Note that no change of linear regime is visible in figure 5(f), meaning that the flat band limit is not yet reached. As a consequence, a value of the order of 20 meV can be considered as an upper limit of the intrinsic Schottky barrier for the Co contacts based device. As shown in figure 6(f), the behavior of φ_B as a function of V_G for the Pd contacts based device is quite different. We do not report any dependence of the injection barrier as a function of the gate voltage. Note that given the difference of SiO_2 thickness for the two devices (280 nm thick insulating SiO_2 for the Pd contacts based device and 100 nm thick insulating SiO_2 for the Co contacts based devices), a different coupling to the gate electrode is realized in the two cases for the same applied gate voltage, inducing a less effective field effect in the Pd case. In the meanwhile, the barrier height shows an almost constant behavior, within the error bars, that could suggest that the injection process occurs already by tunneling. However, the strong temperature dependence of the current observed in a large range of V_{sd} values ($0.1\ V < V_{sd} < 1\ V$) as shown in figures 5(a) and 6(a) is not in favor of this argument. We suggest that the observed invariance of the barrier height could be a specific signature of Fermi level pinning [60] occurring at the Pd/WSe_2 interface. Very weak variations of the injection barrier height with respect to gate voltage were also reported in MoS_2/Au and $MoTe_2$/Au interfaces where Fermi level pinning have been proved to occur [24]. Several physical mechanisms have been proposed to explain the pinning phenomena at metal/TMD interfaces. Sotthewes and coworkers have put forward the role of metal-induced gap states and of disorder [60]. Gong and coworkers have identified two other contributions in the specific cases of metal/MoS_2 interfaces but that could be potentially transposed to the metal/WSe_2 case: interfacial dipoles and gap states due to the metal/S interaction [61]. Concerning the WSe_2/metal interface, a recent study detailing the chemistry of the Pd/WSe_2 interface demonstrates that WSe_2 remains chemically unperturbed after Pd deposition at room temperature [51]. However, from the electronic structure's point of view, interfacial states dubbed overlap states were predicted by density functional theory to be present at the Fermi energy [31]. They could thus be incriminated in the Fermi level pinning phenomena. Being located at the Fermi energy such hybridized interfacial states can also promote holes injection in WSe_2 by efficiently coupling metallic bands with holes states from the WSe_2. This represents an interesting feature for high performance charge injection in WSe_2. Note that the Fermi level pinning phenomenon is strongly supported by the transfer characteristics of the device with Pd contacts shown in figure 3(c) for which the current varies only weakly with respect to V_G in opposition to the device with Co contacts (unpinned case). An inverted band bending with respect to conventional semiconductor/metal contacts was also predicted at WSe_2/Pd interfaces [31]. Therefore, in the studied Pd devices, one could consider that an unconventional mechanism for the injection occurs. Our results presented in figure 6(f) could be a signature of all those theoretical predictions for transparent contacts [31]. This conclusion is also strongly supported by the linear I_{SD}–V_{SD} characteristics measured at low bias voltages

(<0.2 V) in the Pd-based devices recalling a quasi-ohmic behavior (see figure S1) as reported for Co/h-BN/MoS_2 contacts [54] or $Nb_xW_{1-x}Se_2/WSe_2$ contacts [62].

Concluding remarks

In conclusion, we have characterized holes injection in WSe_2 from two different metals, a metal with strong spin–orbit coupling (Pd) and a ferromagnetic metal (Co). We demonstrated that Pd guarantees very transparent contacts and efficient holes injections in WSe_2 even when no gate voltage is applied, with an almost constant injection barrier and higher current values as a function of the source-drain and the gate voltages. One possible explanation is related to the presence of interfacial states coupling metallic and holes bands from the Pd and the WSe_2 respectively and inducing Fermi level pinning. On the contrary we also showed that Co/WSe_2 contacts can be strongly tuned by applying a back-gate voltage, shifting the injection barrier height down to 20 meV. These results pave the ways for further studies concerning the fundamental aspect of charge and spin injection in WSe_2 in the promising holes transport regime for probing the strong spin–orbit coupling physics.

Materials and methods

Sample preparation

WSe_2 is purchased from HQ Graphene. Bulk crystals are mechanically exfoliated and flakes are deposited on a Si/SiO_2 substrate (100 nm or 280 nm thick) to maximize the optical contrast. The devices are fabricated by defining electrical contacts by e-beam lithography using a double layered PMMA process: a 50 K lower layer of PMMA and a 950 K upper layer of PMMA both spin-coated at 4000 RPM. The metallic contacts are deposited under high vacuum (a few 10^{-7} mBar) by e-beam evaporation. They are deposited at very low evaporation rates (0.1 nm s^{-1}). The thicknesses are 5 nm of Ti covered by 95 nm of Au for the device with Ti contacts, and 20 nm of Co and Pd covered with 30 nm of Au for samples with Co contacts and Pd contacts respectively. Scanning electron microscope images of Co (2 nm) deposited on WSe_2 and Pd (2 nm) deposited on WSe_2 are shown in figures S2 and S3. They reveal that the metal film is already continuous at 2 nm of nominal thicknesses. In all the studied devices, the WSe_2 flakes are composed of few layers leading to thicknesses around 3.5–4 nm. In a separate device with Pd contacts supported on h-BN, the field-effect mobility has been measured to be around 21 $cm^2/V.s$ at 300 K and for a charge density around 1.10^{13} cm^{-2} (see figure S4).

Devices measurements

All the devices are measured with a Cryostation from Montana Instruments. All the measurements are performed in dark conditions and under vacuum. Current-voltage measurements are realized by applying to the device a DC voltage from a GS200 from Yokogawa. After passing through the sample, the output DC current is amplified by an I-V converter. The DC output is measured by a digital voltmeter (34401A from Keysight). The gate voltage is a DC voltage and is applied from a GS200 from Yokogawa.

Acknowledgments

We acknowledge C. Manquest and P. Filloux for technical supports within the clean-room of the Laboratoire Matériaux et Phénomènes Quantiques (UMR 7162) at the Université de Paris. This work is supported by the 2DSPIN project from the 'Ville de Paris' Emergence program. This work has been also supported by the Region Ile-de-France in the framework of DIM Nano-K (SMS project).

Conflict of interest

The authors declare that there are no competing interests.

Author contribution

J R, S T and C B performed the experiments, analyzed the data and wrote the manuscript. S S, M L D R and P M participated to the development of the fabrication process. All authors contributed to the interpretation of the data.

ORCID iDs

Jacko Rastikian https://orcid.org/0000-0003-0764-7045
Stéphan Suffit https://orcid.org/0000-0002-7979-5138
Salvatore Timpa https://orcid.org/0000-0001-5133-9707
Pascal Martin https://orcid.org/0000-0003-1010-8421
Philippe Lafarge https://orcid.org/0000-0002-5107-1058
Maria Luisa Della Rocca https://orcid.org/0000-0002-9801
Clément Barraud https://orcid.org/0000-0002-5675-9927

References

[1] Castellanos-Gomez A 2016 Why all the fuss about 2D semiconductors? *Nat. Photonics* **10** 202–4
[2] Velický M and Toth P S 2017 From two-dimensional materials to their heterostructures: an electrochemist's perspective *Appl. Mater. Today* **8** 68–103
[3] Georgiou T *et al* 2013 Vertical field-effect transistor based on graphene–WS_2 heterostructures for flexible and transparent electronics *Nat. Nanotechnol.* **8** 100–3
[4] Shim J, Park H Y, Kang D H, Kim J O, Jo S H, Park Y and Park J H 2017 Electronic and optoelectronic devices based on two-dimensional materials: from fabrication to application *Adv. Electron. Mater.* **3** 1600364
[5] Choi W, Choudhary N, Han G H, Park J, Akinwande D and Lee Y H 2017 Recent development of two-dimensional transition metal dichalcogenides and their applications *Mater. Today* **20** 116–30
[6] Ross J S *et al* 2014 Electrically tunable excitonic light-emitting diodes based on monolayer WSe_2 p–n junctions *Nat. Nanotechnol.* **9** 268–72
[7] Pospischil A, Furchi M M and Mueller T 2014 Solar-energy conversion and light emission in an atomic monolayer p-n diode *Nat. Nanotechnol.* **9** 257–61
[8] Neal A T, Liu H, Gu J and Ye P D 2013 Magneto-transport in MoS_2: phase coherence, spin–orbit scattering, and the hall factor *ACS Nano* **7** 7077–82
[9] Yuan H *et al* 2013 Zeeman-type spin splitting controlled by an electric field *Nat. Phys.* **9** 563–9
[10] Xu M, Liang T, Shi M and Chen H 2013 Graphene-like two-dimensional materials *Chem. Rev.* **113** 3766–98
[11] Wang Q H, Kalantar-Zadeh K, Kis A, Coleman J N and Strano M S 2012 Electronics and optoelectronics of two-dimensional transition metal dichalcogenides *Nat. Nanotechnol.* **7** 699–712
[12] Liu W, Kang J, Sarkar D, Khatami Y, Jena D and Banerjee K 2013 Role of metal contacts in designing high-performance monolayer n-type WSe_2 field effect transistors *Nano Lett.* **13** 1983–90
[13] Lu N, Guo H, Wang L, Wu X and Zeng X C 2014 Van der Waals trilayers and superlattices: modification of electronic structures of MoS_2 by intercalation *Nanoscale* **6** 4566–71
[14] Klein A, Tiefenbacher S, Eyert V, Pettenkofer C and Jaegermann W 2001 Electronic band structure of single-crystal and single-layer WSe_2: influence of interlayer van der Waals interacti *Phys. Rev.* B **64** 205416
[15] Cheiwchanchamnangij T and Lambrecht W R L 2012 Quasiparticle band structure calculation of monolayer, bilayer, and bulk MoS_2 *Phys. Rev.* B **85** 205302
[16] Jiang H 2012 Electronic band structures of molybdenum and tungsten dichalcogenides by the GW approach *J. Phys. Chem.* C **116** 7664–71
[17] Luo Y K, Xu J, Zhu T, Wu G, McCormick E J, Zhan W, Neupane M R and Kawakami R K 2017 Opto-valleytronic spin injection in monolayer MoS_2/few-layer graphene hybrid spin valves *Nano Lett.* **17** 3877–83
[18] Wang Z, Shan J and Mak K F 2017 Valley- and spin-polarized Landau levels in monolayer WSe_2 *Nat. Nanotechnol.* **12** 144–9
[19] Jin C *et al* 2018 Imaging of pure spin-valley diffusion current in WS_2-WSe_2 heterostructures *Science* **360** 893–6
[20] Pradhan N R *et al* 2015 Hall and field-effect mobilities in few layered p-WSe_2 field-effect transistors *Sci. Rep.* **5** 8979
[21] Radisavljevic B, Radenovic A, Brivio J, Giacometti V and Kis A 2011 Single-layer MoS_2 transistors *Nat. Nanotechnol.* **6** 147–50
[22] Kang J, Liu W, Sarkar D, Jena D and Banerjee K 2014 Computational study of metal contacts to monolayer transition-metal dichalcogenide semiconductors *Phys. Rev.* X **4** 031005
[23] Gong C, Colombo L, Wallace R M and Cho K 2014 The unusual mechanism of partial fermi level pinning at metal–MoS_2 interfaces *Nano Lett.* **14** 1714–20
[24] Kim C, Moon I, Lee D, Choi M S, Ahmed F, Nam S, Cho Y, Shin H-J, Park S and Yoo W J 2017 Fermi level pinning at electrical metal contacts of monolayer molybdenum dichalcogenides *ACS Nano* **11** 1588–96
[25] Ouyang B, Xiong S and Jing Y 2018 Tunable phase stability and contact resistance of monolayer transition metal dichalcogenides contacts with metal *npj 2D Mater. Appl.* **2** 13
[26] Domask A C, Cooley K A, Kabius B, Abraham M and Mohney S E 2018 Room temperature van der waals epitaxy of metal thin films on molybdenum disulfide *Cryst. Growth Des.* **18** 3494–501
[27] Prakash A and Appenzeller J 2017 Bandgap extraction and device analysis of ionic liquid gated WSe_2 Schottky barrier transistors *ACS Nano* **11** 1626–32
[28] Prakash A, Ilatikhameneh H, Wu P and Appenzeller J 2017 Understanding contact gating in Schottky barrier transistors from 2D channels *Sci. Rep.* **7** 12596
[29] Zhong H *et al* 2016 Interfacial properties of monolayer and bilayer MoS_2 contacts with metals: beyond the energy band calculations *Sci. Rep.* **6** 21786
[30] Allain A, Kang J, Banerjee K and Kis A 2015 Electrical contacts to two-dimensional semiconductors *Nat. Mater.* **14** 1195–205
[31] Wang Y *et al* 2016 Does p-type ohmic contact exist in WSe2-metal interfaces? *Nanoscale* **8** 1179–91
[32] Das S, Chen H Y, Penumatcha A V and Appenzeller J 2013 High performance multilayer MoS_2 transistors with scandium contacts *Nano Lett.* **13** 100–5
[33] Fang H, Chuang S, Chang T C, Takei K, Takahashi T and Javey A 2012 High-performance single layered WSe_2p-FETs with chemically doped contacts *Nano Lett.* **12** 3788–92

[34] Tosun M, Chuang S, Fang H, Sachid A B, Hettick M, Lin Y, Zeng Y and Javey A 2014 High-gain inverters based on WSe_2 complementary field-effect transistors *ACS Nano* **8** 4948–53
[35] Movva H C P, Rai A, Kang S, Kim K, Fallahazad B, Taniguchi T, Watanabe K, Tutuc E and Banerjee S K 2015 High-mobility holes in dual-gated WSe_2 field-effect transistors *ACS Nano* **9** 10402–10
[36] Xiao D, Liu G B, Feng W, Xu X and Yao W 2012 Coupled spin and valley physics in monolayers of MoS_2 and other group-VI dichalcogenides *Phys. Rev. Lett.* **108** 196802
[37] Benameur M M, Radisavljevic B, Héron J S, Sahoo S, Berger H and Kis A 2011 Visibility of dichalcogenide nanolayers *Nanotechnology* **22** 125706
[38] Li H, Wu J, Huang X, Lu G, Yang J, Lu X, Xiong Q and Zhang H 2013 Rapid and reliable thickness identification of two-dimensional nanosheets using optical microscopy *ACS Nano* **7** 10344–53
[39] Wang J I J, Yang Y, Chen Y A, Watanabe K, Taniguchi T, Churchill H O H and Jarillo-Herrero P 2015 Electronic transport of encapsulated graphene and WSe_2 devices fabricated by pick-up of prepatterned hBN *Nano Lett.* **15** 1898–903
[40] Cadiz F *et al* 2017 Excitonic linewidth approaching the homogeneous limit in MoS_2-based van der Waals heterostructures *Phys. Rev.* X **7** 021026
[41] Wierzbowski J *et al* 2017 Direct exciton emission from atomically thin transition metal dichalcogenide heterostructures near the lifetime limit *Sci. Rep.* **7** 12383
[42] Terrones H *et al* 2014 New first order Raman-active modes in few layered transition metal dichalcogenides *Sci. Rep.* **4** 4215
[43] Sahin H, Tongay S, Horzum S, Fan W, Zhou J, Li J, Wu J and Peeters F M 2013 Anomalous Raman spectra and thickness-dependent electronic properties of WSe_2 *Phys. Rev.* B **87** 165409
[44] Zhang X, Tan Q H, Bin W J, Shi W and Tan P H 2016 Review on the Raman spectroscopy of different types of layered materials *Nanoscale* **8** 6435–50
[45] Li X L, Qiao X F, Han W P, Zhang X, Tan Q H, Chen T and Tan P H 2016 Determining layer number of two-dimensional flakes of transition-metal dichalcogenides by the Raman intensity from substrates *Nanotechnology* **27** 145704
[46] Tonndorf P *et al* 2013 Photoluminescence emission and Raman response of monolayer MoS_2, $MoSe_2$, and WSe_2 *Opt. Express* **21** 4908
[47] Zhao W, Ghorannevis Z, Chu L, Toh M, Kloc C, Tan P-H and Eda G 2013 Evolution of electronic structure in atomically thin sheets of WS_2 and WSe_2 *ACS Nano* **7** 791–7
[48] Liu Y, Stradins P and Wei S 2016 Van der Waals metal—semiconductor junction : weak Fermi level pinning enables effective tuning of Schottky barrier *Sci. Adv.* **2** e1600069
[49] Eastman D E 1970 Photoelectric work functions of transition, rare-earth, and noble metals *Phys. Rev.* B **2** 1–2
[50] Anwar A, Nabet B, Culp J and Castro F 1999 Effects of electron confinement on thermionic emission current in a modulation doped heterostructure *J. Appl. Phys.* **85** 2663–6
[51] Smyth C M *et al* 2019 Engineering the palladium–WSe_2 interface chemistry for field effect transistors with high-performance hole contacts *ACS Appl. Nano Mater.* **2** 75–88
[52] Wang Z, Li Q, Chen Y, Cui B, Li Y, Besenbacher F and Dong M 2018 The ambipolar transport behavior of WSe_2 transistors and its analogue circuits *NPG Asia Mater.* **10** 703–12
[53] Kim G-S, Kim S-H, Park J, Han K H, Kim J and Yu H-Y 2018 Schottky barrier height engineering for electrical contacts of multilayered MoS_2 transistors with reduction of metal-induced gap states *ACS Nano* **12** 6292–300
[54] Cui X *et al* 2017 Low-temperature ohmic contact to monolayer MoS_2 by van der Waals bonded Co/h -BN electrodes *Nano Lett.* **17** 4781–6
[55] Townsend N J, Amit I, Craciun M F and Russo S 2018 Sub 20 meV Schottky barriers in metal/$MoTe_2$ junctions *2D Mater.* **5** 025023
[56] Wang W, Liu Y, Tang L, Jin Y, Zhao T and Xiu F 2015 Controllable Schottky barriers between MoS2 and permalloy *Sci. Rep.* **4** 6928
[57] Kim Y *et al* 2016 Alloyed 2D metal–semiconductor heterojunctions: origin of interface states reduction and schottky barrier lowering *Nano Lett.* **16** 5928–33
[58] Allain A and Kis A 2014 Electron and hole mobilities in single-layer WSe_2 *ACS Nano* **8** 7180–5
[59] Appenzeller J, Knoch J, Derycke V, Martel R, Wind S and Avouris P 2002 Field-modulated carrier transport in carbon nanotube transistors *Phys. Rev. Lett.* **89** 126801
[60] Sotthewes K, van Bremen R, Dollekamp E, Boulogne T, Nowakowski K, Kas D, Zandvliet H J W and Bampoulis P 2019 Universal Fermi-level pinning in transition-metal dichalcogenides *J. Phys. Chem.* C **123** 5411–20
[61] Gong C, Colombo L, Wallace R M and Cho K 2014 The unusual mechanism of partial fermi level pinning at metal–MoS_2 interfaces *Nano Lett.* **14** 1714–20
[62] Chuang H-J, Chamlagain B, Koehler M, Perera M M, Yan J, Mandrus D, Tománek D and Zhou Z 2016 Low-resistance 2D/2D ohmic contacts: a universal approach to high-performance WSe_2, MoS_2, and $MoSe_2$ transistors *Nano Lett.* **16** 1896–902